



**HAL**  
open science

## Mechanisms of pore formation in hydrogel scaffolds textured by freeze-drying

Jérôme Grenier, Hervé Duval, Fabrice Barou, Pin Lu, Bertrand David, Didier Letourneur

► **To cite this version:**

Jérôme Grenier, Hervé Duval, Fabrice Barou, Pin Lu, Bertrand David, et al.. Mechanisms of pore formation in hydrogel scaffolds textured by freeze-drying. *Acta Biomaterialia*, 2019, 94, pp.195-203. 10.1016/j.actbio.2019.05.070 . hal-02144830

**HAL Id: hal-02144830**

**<https://hal.science/hal-02144830>**

Submitted on 27 May 2020

**HAL** is a multi-disciplinary open access archive for the deposit and dissemination of scientific research documents, whether they are published or not. The documents may come from teaching and research institutions in France or abroad, or from public or private research centers.

L'archive ouverte pluridisciplinaire **HAL**, est destinée au dépôt et à la diffusion de documents scientifiques de niveau recherche, publiés ou non, émanant des établissements d'enseignement et de recherche français ou étrangers, des laboratoires publics ou privés.

1 **Mechanisms of pore formation in hydrogel scaffold**  
2 **textured by freeze-drying**

3  
4 Jérôme Grenier <sup>a, b, c</sup>, Hervé Duval <sup>a, \*</sup>, Fabrice Barou <sup>d</sup>, Pin Lv <sup>e</sup>, Bertrand David <sup>b, 1</sup> and Didier  
5 Letourneur <sup>c, 1</sup>

6  
7 <sup>a</sup> Laboratoire LGPM, CentraleSupélec, Université Paris-Saclay, Gif-sur-Yvette, 91190, France

8 <sup>b</sup> Laboratoire MSSMat, UMR 8579 - CentraleSupélec, Université Paris-Saclay, Gif-sur-Yvette,  
9 91190, France

10 <sup>c</sup> Université de Paris, Université Paris 13, INSERM 1148, LVTS, Hôpital Bichat, F-75018  
11 Paris, France

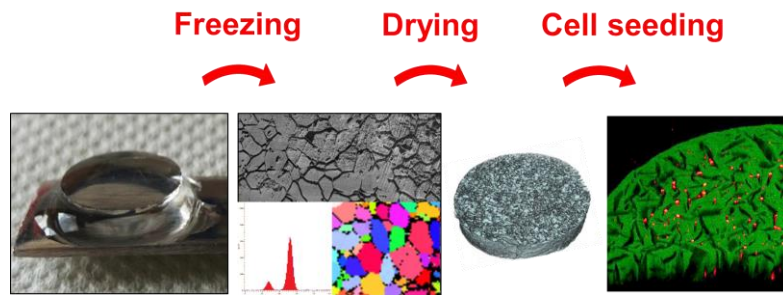
12 <sup>d</sup> Géosciences Montpellier, UMR 5243, Université Montpellier, CNRS, Montpellier Cedex 05,  
13 34095, France

14 <sup>e</sup> LGPM, CentraleSupélec, SFR Condorcet FR CNRS 3417, Université Paris-Saclay, Centre  
15 Européen de Biotechnologie et de Bioéconomie (CEBB), 3 rue des Rouges Terres 51110  
16 Pomacle, France

17 \* Corresponding author: [herve.duval@centralesupelec.fr](mailto:herve.duval@centralesupelec.fr)

18 <sup>1</sup> equal last authors

19 **Graphical Abstract**



20

21

22 **Keywords**

23 Polysaccharide-based hydrogel; Ice-templating; Freeze-drying; Porous scaffolds; 3D cell  
24 culture

25

26 **Statement of significance**

27 The fabrication of hydrogel scaffolds is an important research area in tissue engineering.  
28 Hydrogels are textured to provide a 3D-framework that is favorable for cell proliferation and/or  
29 differentiation. Optimum hydrogel pore size depends on its biological application. Producing  
30 porous hydrogels is commonly achieved through freeze-drying. However, the mechanisms of  
31 pore formation remain to be fully understood. We carefully analyzed scaffolds of a cross-linked  
32 polysaccharide-based hydrogel developed for bone tissue engineering, using state-of-the-art  
33 microscopic techniques. Our experimental results evidenced the shaping of hydrogel during  
34 the freezing step, through a specific ice-templating mechanism. These findings will guide the  
35 strategies for controlling the porous structure of hydrogel scaffolds.

36

37 **Abstract**

38 Whereas freeze-drying is a widely used method to produce porous hydrogel scaffolds, the  
39 mechanisms of pore formation involved in this process remained poorly characterized. To  
40 explore this, we focused on a cross-linked polysaccharide-based hydrogel developed for bone  
41 tissue engineering. Scaffolds were first swollen in 0.025% NaCl then freeze-dried at low  
42 cooling rate, i.e.  $-0.1\text{ }^{\circ}\text{C min}^{-1}$ , and finally swollen in aqueous solvents of increasing ionic  
43 strength. We found that scaffold's porous structure is strongly conditioned by the nucleation  
44 of ice. Electron cryo-microscopy of frozen scaffolds demonstrates that each pore results from  
45 the growth of one to a few ice grains. Most crystals were formed by secondary nucleation since  
46 very few nucleating sites were initially present in each scaffold ( $0.1\text{ nuclei cm}^{-3}\text{ }^{\circ}\text{C}^{-1}$ ). The  
47 polymer chains are rejected in the intergranular space and form a macro-network. Its  
48 characteristic length scale coincides with the ice grain size ( $160\text{ }\mu\text{m}$ ) and is several orders of  
49 magnitude greater than the mesh size ( $90\text{ nm}$ ) of the cross-linked network. After sublimation,  
50 the ice grains are replaced by macro-pores of  $280\text{ }\mu\text{m}$  mean size and the resulting dry structure  
51 is highly porous, i.e. 93%, as measured by high-resolution X-ray tomography. In the swollen  
52 state, the scaffold mean pore size decreases in solvent of increasing ionic strength ( $120\text{ }\mu\text{m}$  in  
53 0.025% NaCl and  $54\text{ }\mu\text{m}$  in DBPS) but the porosity remains the same, i.e. 29% regardless of  
54 the solvent. Finally, cell seeding of dried scaffolds demonstrates that the pores are adequately  
55 interconnected to allow homogenous cell distribution.

56

## 57 **1. Introduction**

58 Biocompatible hydrogel scaffolds have recently gained increasing interest in tissue engineering  
59 [1], with manufacturing suitable scaffolds for cell culture and tissue regeneration remaining an  
60 intensive area of development since the early 80s [2]. Cell attachment, viability [3] and  
61 migration [4] are strongly correlated with pore size. Porous matrix can be produced by various  
62 methods such as fiber bonding, salt leaching, foaming and 3D printing [5]. Freeze-drying (**Fig.**  
63 **2**) is a versatile method for producing porous hydrogels [6]. Two manufacturing routes are  
64 reported in the literature: (1) a polymeric solution is cross-linked and then freeze-dried, or (2)  
65 a polymeric solution is freeze-dried and then cross-linked or coprecipitate [7]. Whatever the  
66 route, the final texture strongly depends on the cooling rate during the cooling step. During this  
67 stage, the free water and possibly part of the bound water transform into ice [8]. This phase  
68 transition is referred to as freezing or solidification. In the case of low cooling rate, equiaxed  
69 solidification of water leads to 3D homogenous structure [9]. Quenching in liquid nitrogen  
70 [10], or unidirectional freezing technologies [11–13], on the contrary, favor columnar  
71 solidification of water leading to 2D ordered tubular structure with aligned channel pores,  
72 which has an average spacing that is dependent on the cooling rate. However, quenching in  
73 liquid nitrogen or unidirectional freezing are less scalable than standard freeze-drying at a low  
74 cooling rate.

75 Water solidification within hydrogel takes place in two stages, *i.e.*, nucleation in supercooled  
76 water followed by ice growth at a temperature near the ice melting point (**Fig. 2**). Ice acts as a  
77 porogen. This process called the ice-templating has been primarily studied for colloid  
78 suspensions [14], but to a much lesser extent for polymer hydrogels. Since the polymer  
79 solubility is lower in ice than in liquid water, the polymer chains are rejected by the growing  
80 ice crystals and then form a continuous macro-network or super-network that interpenetrates  
81 the ice network on the ice grain scale [15]. The term “grain” refers to a crystal surrounded by

82 other crystals and implies the existence of grain boundaries that hold the grains together. For  
83 clarification, the use of the more general term “crystal” is here restricted to isolated crystals.

84 The scenario described above has been first advanced for the Manufacturing Route 2 but never  
85 evidenced. Furthermore, its relevance for Route 1 is not straightforward since the polymer is  
86 cross-linked before the freezing step.

87 To explain how water solidification conditioned the application properties of cross-linked  
88 hydrogels, we raised the following issues: First, the ice network and the segregation of the  
89 polymer chains on the ice grain boundary network have never been observed. Second, the  
90 characterization of the porous structure is most often carried out in 2D which gives a biased  
91 interpretation [12]. Last, the use of the dried structure in cell culture conditions needs to be  
92 further examined. In this work, we address the mechanisms of pore formation by freeze-drying  
93 in a polysaccharide-based hydrogel scaffold designed for bone tissue engineering [16]. This  
94 biomaterial is under research and industrial developments [17–21]. The scaffolds are  
95 manufactured according to Route 1 with a low cooling rate. For the first time, the sketch of  
96 water solidification within the hydrogel scaffold was revealed by Electron Backscattering  
97 Diffraction (EBSD) coupled with Energy-Dispersive X-ray spectroscopy (EDX) at -100°C.  
98 EBSD is a very powerful technique for the characterization of crystalline microstructures in  
99 the scanning electron microscope. It can provide accurate and quantitative data to analyze  
100 microstructure of the materials, e.g. sizes and morphology of individual grains, crystal  
101 orientation... The technique can now be used to analyzing ice at -100°C [22,23]. After freeze-  
102 drying, the porous structure of the scaffolds was analyzed in its entirety in 3D with high-  
103 resolution microscopy (X-ray tomography). The porous structure in cell culture conditions was  
104 then investigated with Confocal Laser Scanning Microscopy (CLSM). Finally, an in-depth  
105 analysis of the experimental results provided a clear picture of the mechanisms underlying the

106 formation and the evolution of pores within cross-linked hydrogel scaffold. These findings will  
107 help to control and optimize the porous structure of hydrogel scaffold.

108

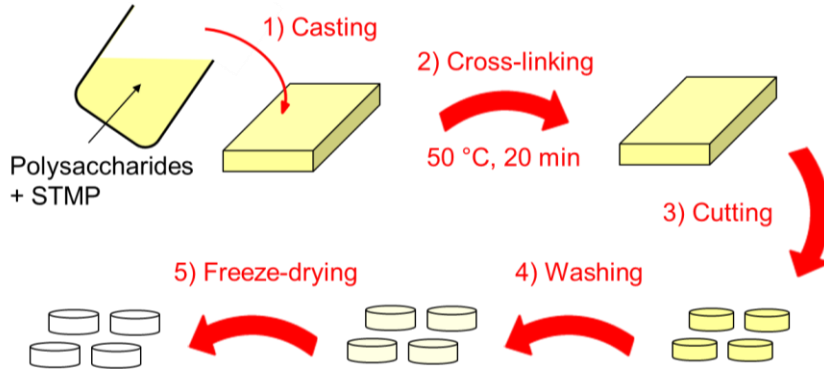
## 109 **2. Materials and methods**

### 110 **2.1 Polysaccharides**

111 Pullulan 200 kDa (Hayashibara, Okayama, Japan) and dextran 500 kDa (Pharmacosmos,  
112 Holbaek, Denmark) were used in this study. Solutions of pullulan or dextran ( $10 \text{ g L}^{-1}$ ) in  
113  $\text{NaNO}_3$  ( $0.15 \text{ mol L}^{-1}$ ) were analyzed using size exclusion chromatography with HPLC  
114 equipped with PWxl Guard-column (TSK-GEL<sup>®</sup>) operated at  $0.5 \text{ mL min}^{-1}$ . Number and mass  
115 average molecular weights (resp.  $M_n$  and  $M_w$ ), polydispersity ( $I_p$ ) and gyration radius ( $R_n$ ) were  
116 computed with light scattering instrument TREOS (Wyatt Technology) using  $0.14 \text{ mL g}^{-1}$   
117 refractive-index increment and 657 nm wavelength.

### 118 **2.2 Hydrogel formulation**

119 The polysaccharide-based hydrogel was synthesized with an aqueous solution of  
120 polysaccharides (75% pullulan – 25 % dextran (w/w),  $0.3 \text{ g mL}^{-1}$ ) containing NaCl ( $0.35 \text{ g mL}^{-1}$ )  
121 <sup>1</sup>) according to published protocols [16,24]. Sodium trimetaphosphate (STMP) solution ( $0.3 \text{ g}$   
122  $\text{mL}^{-1}$ ) was added under alkaline conditions obtained after the addition of NaOH solution ( $10$   
123  $\text{mol L}^{-1}$ ). Final solution contained  $16.5 \text{ \% g-STMP g-polysaccharides}^{-1}$ . The solution was  
124 rapidly cast between glass plates with a 1 mm gap and placed for 20 minutes at  $50 \text{ }^\circ\text{C}$  in an  
125 oven (**Fig. 1**). Scaffolds were formed by disc-cutting (Harris Uni-Core, Sigma Aldrich) at 5  
126 mm in diameter. Scaffolds were then neutralized with Phosphate Buffer Saline solution (10x)  
127 and extensively washed with  $0.025 \text{ \% (g L}^{-1}) \text{ NaCl}$  solution until equilibrium at  $540 \text{ } \mu\text{S cm}^{-1}$ .  
128 Since hydrogel scaffolds were cast in the shape of a cylinder, we use, in the whole text, X and  
129 Y for designating the directions parallel to the cylinder base and Z for its symmetry axis.



130

131 **Fig. 1.** Schematic illustration of the scaffold fabrication process.

132

133 **2.3 Swelling experiments**

134 The volume fraction of the polymer in the relaxed state ( $v_{2r}$ ) and in the swollen state ( $v_{2s}$ ) was  
 135 determined by weighing the hydrogel in the relaxed state ( $W_r$ ) and in the swollen state ( $W_s$ ).

136 The polymer dried weight ( $W_d$ ) was obtained after extensive washing in pure water and 4 days  
 137 at 50°C in a low vacuum chamber.

138 As a first approximation, we neglected the concentration dependence of the partial specific  
 139 volumes of water and polymer and assumed that the hydrogel behaves as an infinitely dilute  
 140 system. The partial specific volume of the polymer mixture ( $v$ ) was estimated at 0.0006125 m<sup>3</sup>  
 141 kg<sup>-1</sup> by mass-averaging the partial specific volumes of dextran and pullulan at infinite dilution  
 142 [25,26]. The partial specific volume of the solvent was taken equal to the specific volume of  
 143 the pure solvent. Then, the volume fractions of the polymer read

$$v_{2r,s} = \frac{W_d v}{((W_{r,s} - W_d)/\rho_{r,s}) + W_d v} \quad (1)$$

144 where  $\rho_r$  is the density of the solvent associated with the relaxed state, i.e. the solvent used for  
 145 cross-linking, and  $\rho_s$  is the density of the solvent associated with the swollen state of the  
 146 polymer. The swelling volume ratio is defined as  $Q = 1/v_{2s}$

147

148

#### 149 2.4 Rheological measurements and mesh size

150 Scaffolds (2 cm in diameter) were analyzed with Discovery HR-2 (TA Instrument®) rheometer  
151 between plan-plan crosshatched geometry. Immersion cup and Peltier plates allowed  
152 equilibrium at 37°C with 0.025 % NaCl. Axial force standardization was achieved by  
153 monitoring axial force against gap reduction until surface leap effect have been overcome [27].  
154 The storage modulus of the hydrogel ( $G'$ ) was determined from the characterization of six  
155 independent samples with no more than 0.1 N axial force at 0.05 % strain (linear domain) and  
156 1 Hz oscillation. The number average molecular weight between cross-links ( $M_c$ ) was deduced  
157 from the storage modulus using the Gaussian rubber elasticity theory modified by Peppas and  
158 Merrill [28,29]:

$$G = \frac{R T C_{2r}}{M_c} \left(1 - \frac{2M_c}{M_n}\right) \left(\frac{v_{2r}}{v_{2s}}\right)^{-\frac{1}{3}} \quad (2)$$

159 where  $R$  is the gas constant ( $\text{J mol}^{-1} \text{K}^{-1}$ ),  $C_{2r}$  is the polymer concentration in the relaxed state  
160 ( $\text{kg m}^{-3}$ ) and  $M_n$  is the number average molecular weight of pullulan – dextran mixture.  
161 Equation (2) is valid if the polymer network behaves as a collection of Gaussian chains.  
162 According to Treloar [28], the regime is Gaussian as long as the relative end-to-end distance  
163 of the network chains remains lower than 0.3. We checked that this condition was actually met  
164 (see the Results section).

165 Since there is no model of end-to-end distance for chains made of both pullulan and dextran,  
166 the end-to-end distance of the chains in the unperturbed state,  $(\overline{r_0^2})^{\frac{1}{2}}$ , was estimated under 100%  
167 pullulan and 100% dextran assumption. Furthermore, we neglected the effect of the  
168 monolinked phosphate on the end to end distance. The number average molecular weight  
169 between cross-links under 100% pullulan (resp. dextran) assumption, denoted  $M_c^{pul}$  (resp.

170  $M_c^{dex}$ ), was thus calculated from equation (2) with  $M_n^{pul}$  (resp.  $M_n^{dex}$ ). Then, the end-to-end  
 171 distance was estimated for pullulan following:  $(\overline{r_0^2})^{\frac{1}{2}} \cong l \left( (M_c^{pul} / M_r) C_\infty \right)^{\frac{1}{2}}$  with alpha-D-  
 172 glucose residue as repeating unit ( $M_r = 162 \text{ g mol}^{-1}$ ),  $l = 4.79 \text{ \AA}$  and  $C_\infty = 4.3$  according to  
 173 Buliga and Brant [30]. For dextran, the end-to-end distance was computed following:  $(\overline{r_0^2})^{\frac{1}{2}} =$   
 174  $0.071 \sqrt{M_c^{dex}}$  according to İmren et al. [25]. The mesh size in the swollen state was estimated  
 175 for dextran chains and pullulan chains with equation (3) according to Canal and Peppas [31]:

$$\xi = \alpha (\overline{r_0^2})^{\frac{1}{2}} \quad (3)$$

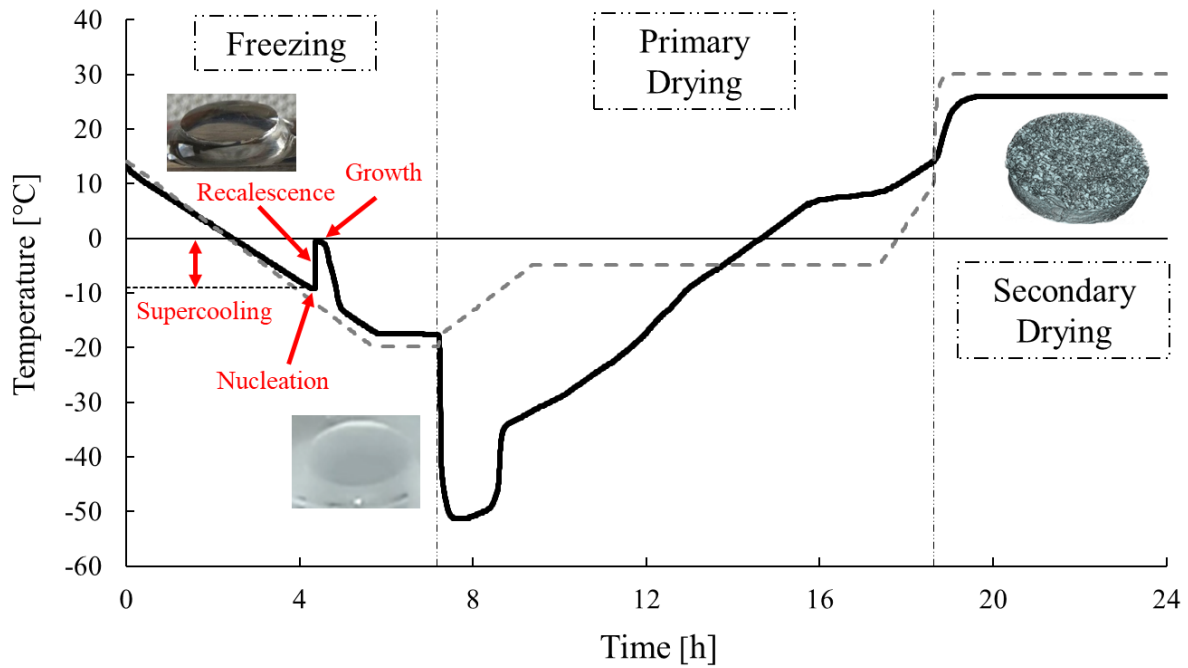
176 **where  $\alpha$  is the elongation ratio of the polymer chain.** Following Canal and Peppas [31], we  
 177 assumed that the hydrogel is isotropically swollen.  $\alpha$  is then related to the swollen polymer  
 178 volume fraction,  $v_{2s}$ , by:

$$\alpha = v_{2s}^{-\frac{1}{3}} \quad (4)$$

179

## 180 2.5 Freeze-drying process

181 Scaffolds (11 mm in diameter, 2 mm in height) swollen in 0.025% NaCl (and drained to remove  
 182 the solvent excess) were disposed in Petri dishes (VWR, 391-0875) and placed on freeze-dryer  
 183 trays (MUT 004, Cryotec®). Scaffolds axis was systematically oriented perpendicular to the  
 184 tray. The freeze-drying protocol consists of three stages (**Fig. 2**). Cooling runs under  
 185 atmospheric pressure at a constant rate of  $-0.1 \text{ }^\circ\text{C min}^{-1}$  from  $15 \text{ }^\circ\text{C}$  to  $-20 \text{ }^\circ\text{C}$  followed by a  
 186 phase at constant temperature of  $-20 \text{ }^\circ\text{C}$  during 90 min. Primary drying occurs at low pressure  
 187 (0.010 mbar) and  $-5 \text{ }^\circ\text{C}$  for 8 h and secondary drying at  $30 \text{ }^\circ\text{C}$  for 1 hour.



188

189 **Fig. 2.** Freeze-drying of hydrogel scaffolds. The process comprises three stages: freezing,  
 190 primary drying and secondary drying. Black line: scaffolds temperature; grey dashed line: plate  
 191 temperature. Here, supercooling is followed by nucleation at  $-9\text{ }^{\circ}\text{C}$ .

192

## 193 2.6 Dedicated nucleation experiments

194 In order to identify the nucleation mechanisms that are in play during freeze-drying, a series of  
 195 at least 36 independent scaffolds swollen in 0.025% NaCl (10 mm in diameter) were frozen in  
 196 Petri dishes on freeze-dryer trays (MUT 004, Cryotec®). The scaffolds were separated from  
 197 each other by no less than two diameters. The constant cooling rate of  $-0.2\text{ }^{\circ}\text{C min}^{-1}$  was  
 198 applied. The number of unfrozen samples,  $N(t)$  was recorded every minute and associated with  
 199 the freeze-dryer plate temperature. We then considered that the nucleation temperature of a  
 200 scaffold coincides with the plate temperature at the onset of its freezing.

201 Moreover, a dedicated cooling protocol was applied on 98 scaffolds according to Vali [32] with  
 202  $-0.2\text{ }^{\circ}\text{C min}^{-1}$  cooling rate from  $15\text{ }^{\circ}\text{C}$  to  $-15\text{ }^{\circ}\text{C}$ , then a phase at  $-14\text{ }^{\circ}\text{C}$  for 30 minutes and

203 eventually cooling at  $-0.2\text{ }^{\circ}\text{C min}^{-1}$  rate until  $-20^{\circ}\text{C}$ . We determined the variations of the  
 204 freezing rate,  $R$ , as a function of time.  $R$  is defined as the ratio of the number of freezing  
 205 scaffolds per minute to the number of unfrozen ones [32]. It was derived from the variations  
 206 of  $N$ :

$$R(t) = - \frac{N(t + \Delta t) - N(t - \Delta t)}{2\Delta t} \frac{1}{N(t)} \quad (5)$$

207 with  $\Delta t = 2\text{ min}$ .

208 We found that the exponential function well fits the variations of  $R$  as a function of time (**Fig.**  
 209 **3B**). Because cooling rate is constant, we deduced that the variations of  $R$  as a function of  
 210 temperature may be expressed as

$$R = R(T) = ae^{-bT} \quad (6)$$

211 Assuming singular hypothesis for nucleation, we determined the so-called differential nucleus  
 212 concentration,  $k(T)$ , as defined by Vali [32].  $k(T)$  represents the concentration of nuclei per unit  
 213 volume with activation temperature within one degree. It is then given by

$$k(T) = - \frac{R(T)}{V r} \quad (5)$$

214 where the cooling rate  $r = -0.2^{\circ}\text{C min}^{-1}$  and the scaffold volume  $V = 0.2 \pm 0.02\text{ cm}^3$ .

215

## 216 2.7 Scanning electron microscopy of frozen scaffolds

217 The scaffolds were collected at the end of cooling stage at  $-20^{\circ}\text{C}$  before primary drying. The  
 218 samples were stored at  $-80^{\circ}\text{C}$  until further use. The CamScan Crystal Probe X500FE SEM-  
 219 EBSD (CNRS UMR 5243, University of Montpellier), equipped with C1001 GATAN gaseous  
 220 nitrogen cold stage modulus was used to perform the analysis in cold conditions as described  
 221 previously [22,23]. Briefly, samples preparation was conducted in a freezer at  $-60^{\circ}\text{C}$  by  
 222 polishing the surface with cryotome blade just before the analysis. In the chamber, the sample

223 was maintained between  $-90\text{ }^{\circ}\text{C}$  and  $-100\text{ }^{\circ}\text{C}$  with 1 Pa vacuum. EBSD was performed with  
224  $20\text{ }\mu\text{m}$  step size and 20 Hz acquisition speed concomitantly with EDX. Operating conditions  
225 were 20 kV acceleration voltage and 25 mm working distance. Aztec software package from  
226 Oxford Instruments HKL was used to index EBSD pattern and align with EDX spectra.  
227 Indexation of ice crystal from hexagonal space group 186 with  $a = 4.51\text{ }\text{\AA}$  and  $c = 7.34\text{ }\text{\AA}$  was  
228 successful over more than 90 % of the surface with less than  $0.5^{\circ}$  angular resolution. Channel5  
229 software package was used to process EBSD patterns into Inverse Pole Figures (IPF)  
230 orientation map and pole figures. Ice grains were defined as continuous domains with less than  
231  $10^{\circ}$  crystallographic misorientation. Ice grain size was defined as the square root of grain area.

## 232 2.8 Porous structure analyses of freeze-dried scaffolds

233 The 3D architecture of freeze-dried scaffolds with a voxel size of  $(6\text{ }\mu\text{m})^3$  was acquired by X-  
234 ray nanotomograph EasyTom XL 150/160 (RX-solutions, France) using a sealed micro-focus  
235 tube at a working voltage of 50 kV and a working current of  $120\text{ }\mu\text{A}$ . An amorphous silicon  
236 matrix plan (ASMP) detector of  $1920 \times 1536$  pixels was used and 1440 radiographs were  
237 obtained with an exposure time of 0.2 s and an averaging of 10. The image reconstruction,  
238 performed on a server with 4 GPU cards (Nvidia GTX1080), requires ca. 2 minutes. By  
239 building up the generated 2D slice images, the 3D volume of the sample was achieved using  
240 Avizo®.

241 CLSM (ZEISS LSM700) was used to explore the 3D porous structure of swollen scaffolds  
242 labelled with 0.17% (w/w) 500 kDa FITC-dextran (TdB Consultancy) during formulation.  
243 After freeze-drying, scaffolds were allowed to swell overnight in 0.025% (w/v) NaCl. XZ  
244 views (where Z is the symmetry axis of the scaffold) were acquired over  $250\text{-}\mu\text{m}$  depth in 43  
245 confocal slices of  $2.5\text{ }\mu\text{m}$  pixel size after cutting the swollen scaffolds with razor blade  
246 (0.12HD, ASR). Two-photon microscope (LEICA, SP8) was used to acquire scaffold swollen  
247 in DPBS (Gibco, SigmaAldrich) over  $250\text{-}\mu\text{m}$  depth in 13 slices with  $0.692\text{ }\mu\text{m}$  pixel size.

248 Pores are defined as objects of air or liquid delimited by dried (or hydrated) cross-linked  
249 polysaccharides. Pores were isolated in 3D with Aviso software (Thermo Scientific™) after  
250 thresholding, holes filling, object separation (watershed algorithm) and labelling. The pore size  
251 was defined as the cubic root of the 3D pore volume. Aviso software provided the geometric  
252 orientation of the pores. Polar angle ( $\varphi$ ) and azimuthal angle ( $\theta$ ) defined the main axis  
253 orientation of an equivalent ellipsoid in 3D for each pore.

## 254 2.9 Cell seeding in freeze-dried hydrogel scaffold

255 MC3T3-E1 pre-osteoblasts cells were cultivated in  $\alpha$ -MEM medium with nucleosides without  
256 ascorbic acid (GIBCO, A1049001) supplemented with 10% FBS (GIBCO, 10270-106) in  
257 standard cell culture conditions. Cell membrane labelling was performed with PKH-26 dye  
258 (Phanos Technologies) according to manufacturer protocol. 20  $\mu$ L of cell suspension ( $5 \times 10^6$   
259  $\text{mL}^{-1}$ ) was added directly on freeze-dried hydrogel scaffold. Complete swelling was allowed  
260 by regular addition of the medium. The scaffolds were then incubated in standard cell culture  
261 conditions during 24 h in 6-well plate with 1.5 mL of medium and 4 scaffolds per well. XZ  
262 views to 250- $\mu\text{m}$  depth were acquired with CSLM. Hydrogel green signal (FITC dextran) and  
263 cell red signal (PKH-26) were recorded on two channels. Cells clusters were analyzed with 3D  
264 Object Counter (Fidji, Java Software).

## 265 2.10 Statistical methods

266 Values are given as mean  $\pm$  standard deviation. Analysis of variance and Student's *t*-test  
267 assessed significance of data (Microsoft Excel, 2016). In figures, error bars correspond to  
268 standard deviation. Regression analysis was performed with Monte Carlo algorithm (R Core  
269 Team, 2016).

270

271

## 272 3. Results

### 273 3.1 Cross-linking and subsequent mesh size of the polysaccharide-based hydrogel

274 The characteristics of the starting polymers were determined by light scattering measurements,  
275 i.e.  $M_n^{pul} = 158.8 \text{ kg mol}^{-1}$ ,  $I_p = 1.98$  and  $R_n = 17.1 \pm 0.8 \text{ nm}$  for pullulan, and  $M_n^{dex} = 284.9 \text{ kg}$   
276  $\text{mol}^{-1}$ ,  $I_p = 1.82$  and  $R_n = 16.0 \pm 0.8 \text{ nm}$  for dextran. Thus, the number average molecular weight  
277 of the 75/25 mixture is  $M_n = 178.6 \text{ kg mol}^{-1}$ . After cross-linking, the volume fraction of the  
278 polymer in the relaxed state (i.e. the polymer kept in the solvent used for cross-linking) is equal  
279 to  $v_{2r} = 0.11$ . Swelling in 0.025% (w/v) NaCl solution results in a swelling volume ratio  $Q =$   
280 80. The volume fraction of the polymer in the swollen state is equal to  $v_{2s} = 0.012$ .

281 Rheological measurements indicate that the hydrogel is incompressible and highly elastic ( $\tan$   
282  $\delta = 0.09$ ). At 37 °C in 0.025 % NaCl with frequency of 1 Hz under 0.05% strain and 0.03 N  
283 axial force, the storage modulus is estimated at  $G' = 0.9 \pm 0.1 \text{ kPa}$ . The average molecular  
284 weight between consecutive cross-links,  $M_c$ , was determined according to the Gaussian rubber  
285 elasticity theory modified by Peppas and Merrill [28], i.e.  $M_c = 68 \text{ kg mol}^{-1}$  for the resulting  
286 hydrogel. Under 100% pullulan and 100% dextran assumption, the average molecular weight  
287 between consecutive cross-links differs slightly, i.e.  $M_c^{pul} = 62 \text{ kg mol}^{-1}$  and  $M_c^{dex} = 95 \text{ kg}$   
288  $\text{mol}^{-1}$ , respectively. Then, the end-to-end distance of the chains in the unperturbed (solvent-  
289 free) state was estimated at  $(\overline{r_0^2})^{1/2} = 19 \text{ nm}$  and  $(\overline{r_0^2})^{1/2} = 22 \text{ nm}$ , respectively. After swelling  
290 in 0.025% NaCl, the mesh size was estimated at  $\zeta = 83 \text{ nm}$  and  $\zeta = 94 \text{ nm}$ , respectively. We  
291 also checked that the chains of the polymer network remain Gaussian: the relative end-to-end  
292 distance of the network chains after swelling in 0.025% NaCl is estimated at about 0.2, under  
293 100% pullulan assumption. The relative extension is thus lower than 0.3 corresponding to the  
294 onset of deviations from the Gaussian statistics.

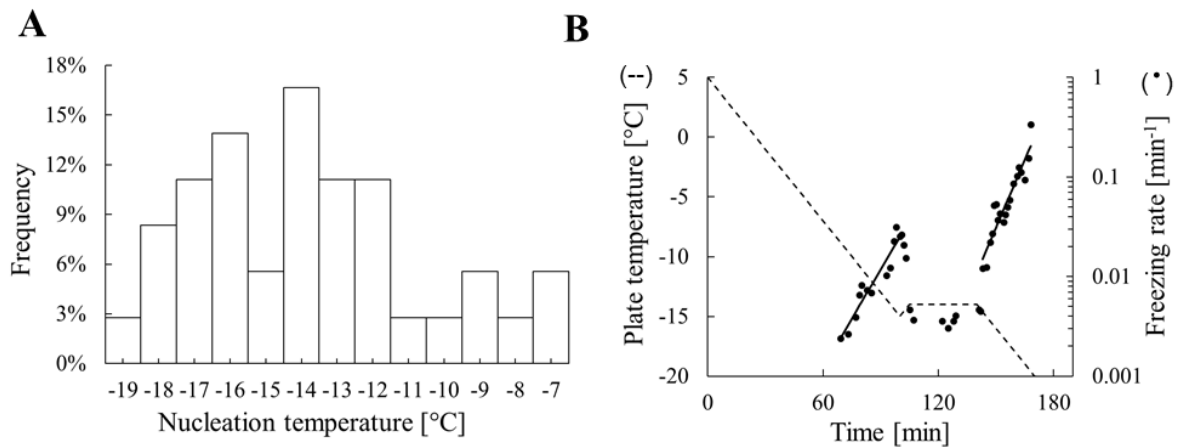
295 We then investigated the fate of the polysaccharide network during and after freeze-drying.

## 3.2 Nucleation of ice from supercooled hydrogel

**Fig. 2** shows that supercooling is followed by nucleation with an abrupt change in opacity during recalescence. Water solidification is achieved close to the ice melting point. In order to characterize the nucleation in the supercooled scaffolds during freeze-drying, series of scaffolds swollen in 0.025% NaCl were cooled at  $-0.2 \text{ }^\circ\text{C min}^{-1}$  rate. **Fig. 3A** shows the nucleation temperature histogram with a mean of  $-13.3 \pm 3 \text{ }^\circ\text{C}$  well above  $-35^\circ\text{C}$ , the homogenous nucleation threshold of pure water [33]. The nucleation is therefore heterogeneous. Heterogeneous nucleation of ice from supercooled water is known to be influenced by two factors, i.e. the properties of the nucleating sites and the growth of embryo to critical size by the random fluctuations [34]. When the former is predominant, nucleation is said to be singular [35]. When the latter prevails, nucleation is stochastic and the classic nucleation theory (CNT) applies. A series of 98 scaffolds was cooled according to the time-temperature pattern similar to Vali [32] in order to discriminate the predominant factor. **Fig. 3B** represents the variations of the freezing rate as a function of time. While temperature decreases for 30 minutes from  $-9^\circ\text{C}$  to  $-15^\circ\text{C}$ , 36.7% of scaffolds freeze, and freezing rate increases exponentially with time (slope of the log-linear plot equal to  $0.076 \pm 0.008 \text{ min}^{-1}$ , R-squared = 0.91). Then, from  $-14^\circ\text{C}$  to  $-20^\circ\text{C}$ , 44.9% of scaffolds freeze, and freezing rate increases exponentially with about the same slope ( $0.1 \pm 0.01 \text{ min}^{-1}$ , R-squared = 0.87). Since the temperature varies linearly with time, we may deduce the differential nucleus concentration, i.e.  $k(T) \cong (3 \times 10^{-4} \pm 2 \times 10^{-4}) \exp[-(0.38 \pm 0.04)T] \text{ nuclei cm}^{-3} \text{ }^\circ\text{C}^{-1}$  valid for  $T \in [-9^\circ\text{C}; -15^\circ\text{C}]$ . This estimate is close to that reported by Vali for water drops [32]. While temperature is kept constant at  $-14 \text{ }^\circ\text{C}$  for 30 minutes, only 5 frozen events occur (5%) even if a large fraction of the scaffolds is still unfrozen. It means that most of the nucleating sites with characteristic temperature higher than  $-14^\circ\text{C}$  have already induced a nucleation event during cooling from  $-9^\circ\text{C}$  to  $-15^\circ\text{C}$ . Thus, there is a depletion of active sites

321 with characteristic temperature close to the plateau temperature ( $-14^{\circ}\text{C}$ ) and freezing rate is  
 322 drastically reduced. This behavior is characteristic of the singular model and cannot be  
 323 explained by the CNT.

324



325

326 **Fig. 3** Characterization of ice nucleation within scaffolds preliminary swollen in 0.025% NaCl  
 327 and submitted to a dedicated cooling protocol. **A:** Histogram of nucleation temperature for a  
 328 batch of 36 scaffolds cooled at  $-0.2^{\circ}\text{C min}^{-1}$ . **B:** Semi-log plot of the freezing rate of a batch  
 329 of 98 scaffolds submitted to a time-temperature pattern similar to Vali [32]: cooling from  $5^{\circ}\text{C}$   
 330 to  $-15^{\circ}\text{C}$  at  $-0.2^{\circ}\text{C min}^{-1}$ , plateau at  $-14^{\circ}\text{C}$  during 30 minutes and cooling from  $-14^{\circ}\text{C}$  to -  
 331  $20^{\circ}\text{C}$  at  $-0.2^{\circ}\text{C min}^{-1}$ .

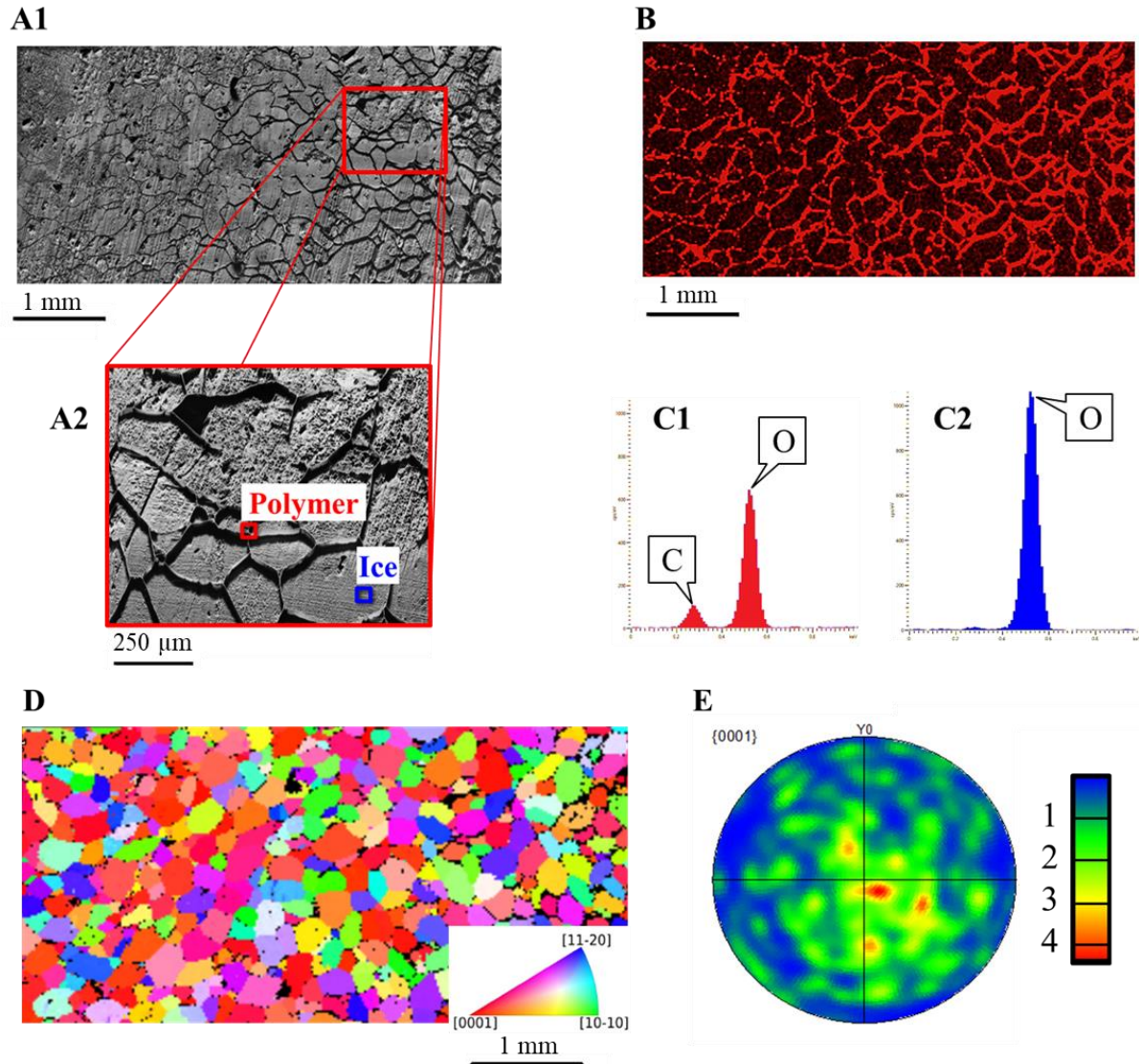
332

333 Following nucleation, ice growth takes place in two stages, i.e. the initial rapid recalcrescent  
 334 stage and the final slower stage close the ice melting point,  $T_m$  [36]. During recalcrescence, the  
 335 ice structure appears as a “milky-white cloud” expanding with a velocity of  $6.5 \pm 3.5 \text{ cm s}^{-1}$  in  
 336 line with findings on water drops [36,37]. Recalcrescence ends when scaffold temperature  
 337 reaches  $T_m$  (temperature increase due to latent heat release). The fraction of frozen water is  
 338 then estimated at  $c_p(T_m - T_n)/L \cong 9\%$  where  $c_p$  is the heat capacity of water,  $L$  the heat of  
 339 fusion and  $T_n$  the nucleation temperature. Freezing is completed at the end of the slower stage.

### 340 3.3 Polycrystalline structure of the frozen hydrogel scaffolds

341 Scanning electron microscopy was performed at  $-100\text{ }^{\circ}\text{C}$  to prevent samples from quick  
342 sublimation. An XY cross-section of a frozen scaffold (nucleation temperature of  $-9.7\text{ }^{\circ}\text{C}$ ) is  
343 shown with topographic contrast on **Fig. 4A**: flat regions of about  $200\text{ }\mu\text{m}$  in length are  
344 surrounded by ridges. The elemental map of **Fig. 4B** shows that carbon is mainly located in the  
345 ridges. EDX spectra of a flat region (labelled “ice”) and a ridge (labelled “polymer”) further  
346 evidenced carbon in the “polymer” region (**Fig. 4C1**), while no significant signal was recorded  
347 for the “ice” region (**Fig. 4C2**). These topographic and chemical analysis prove that the ice  
348 domains are surrounded by polysaccharide. Topography was due to the slight sublimation of  
349 ice under the vacuum of the microscope even at  $-100\text{ }^{\circ}\text{C}$ .

350 EBSD, performed with an Oxford Instruments NordlysNano EBSD detector, was used to  
351 examine the microstructure of the frozen scaffold. Crystal orientation map is displayed in the  
352 so-called Inverse Pole Figure (IPF). In this IPF, ice grains are labelled according to the  
353 measured orientation with respect to the reference direction that is parallel to the scaffold Z  
354 axis (**Fig. 4D**). EBSD data show that water solidified into hexagonal (Ih) ice. Ice is  
355 polycrystalline with an average grain size over 4 preparations found to be  $160 \pm 20\text{ }\mu\text{m}$ . Grains  
356 have equiaxed morphology and texture. However, c-axis pole figure. shows that the highest  
357 pole densities are obtained in and around Z, i.e., at the central region of the pole figure. (**Fig.**  
358 **4E**). Thus, Ih-ice c-axis is preferentially parallel to Z.



359

360 **Fig. 4.** Scanning electron microscopy at  $-100^{\circ}\text{C}$  of a frozen scaffold horizontal cross-section.

361 **A1:** Topography contrast. **A2:** Zoom and definition of labelled areas. **B:** Carbon map obtained

362 by EDX. **C1** and **C2:** EDX spectra of the labelled areas “polymer” and “ice”, respectively. **D:**

363 Z-direction IPF coloring orientation map obtained via EBSD (20  $\mu\text{m}$  step size) and associated

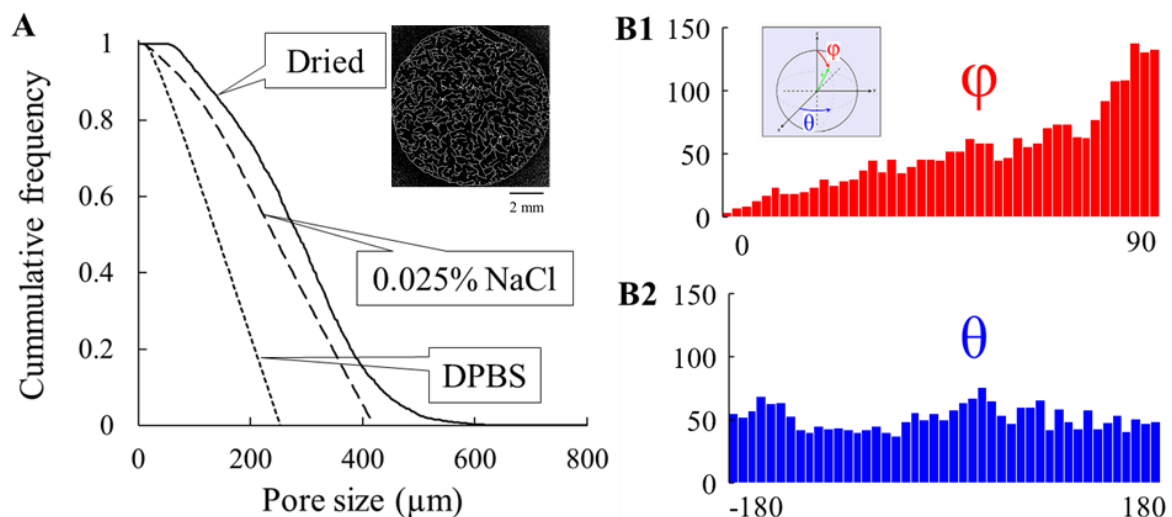
364 IPF key. Red color corresponds to Ih-ice grains with c-axis ([0001]) parallel to Z-direction. **E:**

365 c-axis pole figure.

366 3.4 3D porous structure of freeze-dried scaffold

367 The 3D porous structure of an entire scaffold was analyzed by X-ray computed tomography  
368 with  $(6\ \mu\text{m})^3$  voxel size (**Fig. 5A**). A highly porous structure with very thin walls was observed  
369 similarly to previously reported micro-computed tomography analysis of freeze-dried gels  
370 [38]. After image processing, the porosity was estimated at  $\varepsilon = 93\% \pm 2\%$  and mean pore size  
371 at  $280 \pm 20\ \mu\text{m}$ . About 6% of the pores are micropores ( $<100\ \mu\text{m}$ ) and 94% are macropores  
372 ( $>100\ \mu\text{m}$ ) according to standard nomenclature [39].

373 The distribution of azimuthal and radial orientations of pore major axis indicates that major  
374 axis is preferred parallel to XY plane (distribution of  $\varphi$  maximal close to  $90^\circ$ ) without  
375 preferential orientation in the XY plane (uniform distribution of  $\theta$ ) (**Fig. 5B**).



376

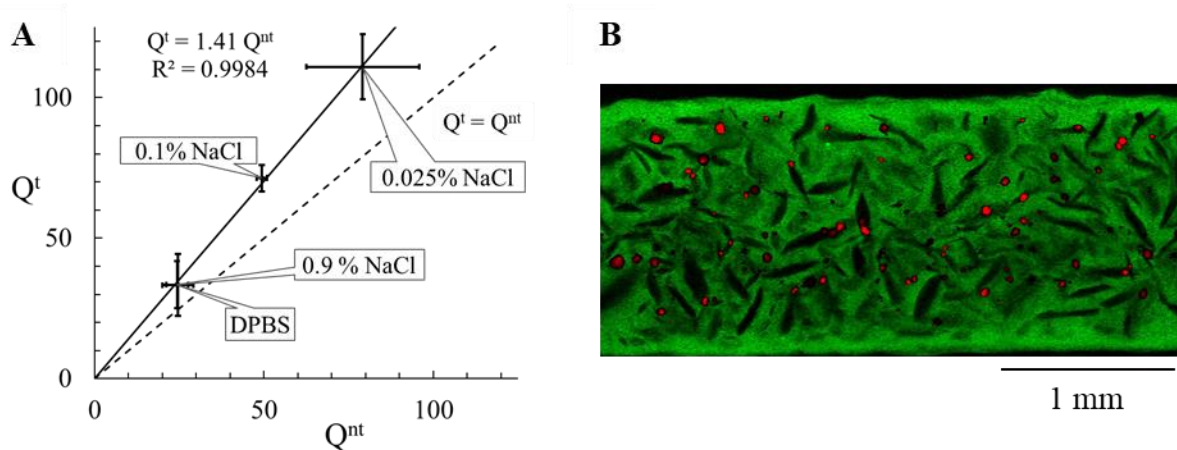
377 **Fig. 5.** 3D assessment of the freeze-dried scaffold porosity. **A:** Pore size cumulative distribution  
378 of an entire scaffold (9.36 mm in diameter, 1.73 mm in height) after freeze-drying (solid line);  
379 scaffolds analyzed to 250- $\mu\text{m}$  depth after swelling in 0.025% NaCl (dash line) and in DPBS  
380 (dotted line). XY slice at 500  $\mu\text{m}$  depth of the X-ray tomography scan with  $(6\ \mu\text{m})^3$  voxel size.

381 **B1** and **B2:** Distribution of polar ( $\varphi$ ) and azimuthal ( $\theta$ ) angles of pore major axis, in the dried  
382 scaffold.

### 383 3.5 Hydrogel porous structure after swelling

384 Hydrogel swelling was investigated for a series of solvents of increasing ionic strength, i.e.  
385 0.025% NaCl, 0.1% NaCl, 0.9% NaCl and Dulbecco's Phosphate Buffer Saline solution  
386 (DPBS) used for cell culture. For each solvent, the swelling volume ratio ( $Q$ ) was determined  
387 for the textured hydrogel (resp. non-textured, i.e. non freeze-dried). **Fig. 6A** shows that for both  
388 textured and non-textured hydrogels, the swelling volume ratio increases as the solvent ionic  
389 strength decreases. This is consistent with the anionic nature of the grafted phosphate [40]. The  
390 swelling ratio of the textured hydrogel,  $Q^t$ , is greater than the swelling ratio of the non-textured  
391 hydrogel,  $Q^nt$ . We found that  $Q^t$  varies linearly with  $Q^nt$ . Since the porosity is given by  $\varepsilon = 1 -$   
392  $(Q^nt/Q^t)$ , we deduce that the porosity of the textured hydrogel in the swollen state is constant  
393 for the tested solvent series and equal to  $\varepsilon = 29\% \pm 2\%$ . Correlatively the pore network varies  
394 homothetically when changing solvent.

395 We further investigated the 3D porous structure of textured hydrogels prepared using FITC-  
396 dextran after swelling in 0.025% NaCl solution using CLSM. The volume of interest was a  
397 slab parallel to Z of 250  $\mu\text{m}$ -thickness. The porosity measured by image analysis was equal to  
398  $\varepsilon = 29\%$ . After pore separation procedure, the mean pore size was estimated at 120  $\mu\text{m}$ . We  
399 can conclude that swelling in 0.025 NaCl% results in pores collapse with the pore size 2.3  
400 times smaller than in the dry state. After swelling in DPBS, textured hydrogel was investigated  
401 using two-photon excitation laser scanning microscopy to minimize scattering in the hydrogel.  
402 The porosity was estimated at  $\varepsilon = 30\%$  and the mean pore size at 54  $\mu\text{m}$ . We thus found that  
403 pore size varies by a scale factor of 2.2 between DPBS and 0.025% NaCl solution, a value  
404 consistent with the scale factor deduced from swelling volume ratio measurements, i.e.  
405  $3.3^{1/3} \cong 1.5$ .



406

407 **Fig. 6.** Fate of the porous structure after swelling and 3D cell culture.

408 **A:** Swelling volume ratio for textured ( $Q_t$ ) and non-textured ( $Q_{nt}$ ) scaffolds swollen in 0.025%  
 409 NaCl, 0.1% NaCl, 0.9% NaCl and DPBS. The linear regression model is fitted to the data  
 410 without the intercept term. **B:** CLSM XZ cross-section of a freeze-dried scaffold (7.2 mm  
 411 diameter, 1.4 mm height) 24 h after the seeding of 100,000 MC3T3-E1 cells.

412

### 413 3.6 Cell seeding demonstrates interconnectivity of pores

414 Dry textured scaffolds were seeded with 100,000 MC3T3-E1 cells previously labelled with  
 415 PKH-26. Clusters were observed 24 h after seeding in the pores, homogenously distributed on  
 416 the scaffold volume (observation to 300- $\mu$ m depth of entire XY sections, see **Fig. 6B** for one  
 417 XZ slice). Our results demonstrate that the pores in the freeze-dried scaffold are adequately  
 418 interconnected to allow homogenous cell distribution. Mean cluster volume was  $81 \times 10^{-3}$   
 419  $\mu$ m<sup>3</sup> corresponding to aggregates of 27 cells in average according to mean MC3T3-E1 volume  
 420 [41]. Interestingly, cluster diameter (53  $\mu$ m) was close to mean pore size (54  $\mu$ m) which  
 421 suggests that cells organized according to the scaffold porous structure.

422

#### 423 **4. Discussion**

424

425 Scaffold freezing is initiated at significant supercooling (about 13°C) by heterogeneous  
426 nucleation. The sites are likely located at the interface between the hydrogel and the plate or  
427 on the polymer network [34]. We found that the heterogeneous nucleation is singular (**Fig. 3B**).  
428 Very few nucleating sites are present in each scaffold (about 0.1 nuclei cm<sup>-3</sup> °C<sup>-1</sup> estimated at  
429 -15°C). During cooling, freezing is triggered by the nucleating site with the highest  
430 characteristic temperature, and the scaffold freezing temperature is equal to the characteristic  
431 temperature of this site [32]. At this temperature, the time needed for an embryo to reach the  
432 critical size is much lower than the cooling characteristic time (instantaneous embryo growth).  
433 Consistently, in a batch of scaffolds, the number of freezing scaffolds per temperature interval  
434 is expected to be almost independent of the cooling rate.

435 At the onset of freezing, growing ice crystals are expected to be needle-like for the present  
436 supercooling values [42]. These needles exhibit a tree-like structure called needled branch [42].  
437 We hypothesized that the rapid growth during the recalescent stage was accompanied by  
438 fragmentation of these needles due to the constraints exerted by the surrounding nano-scale  
439 polymer network. The fragments induces secondary nucleation [43] and the subsequent  
440 equiaxed polycrystalline structure observed on the frozen scaffold with EBSD (**Fig. 4D**). Most  
441 ice grains are formed from secondary nucleation. Since the solubility of the polymer is lower  
442 in ice than in liquid water, the polymer chains are rejected by the growing ice crystals into the  
443 intergranular space and form a macro-network. Simultaneous EDX and EBSD analyses show  
444 that each pore results from the growth of one to a few ice crystals. Since the mesh size of the  
445 polymer network (about 90 nm) is several orders of magnitude lower than the ice grain size  
446 (about 160 µm), polymer exclusion is accompanied by massive chain reorganizations and may  
447 be also by some ruptures of chains or cross-links. X-ray tomography of freeze-dried scaffolds

448 showed that the polymer network remains continuous. Since cell seeding demonstrated that the  
449 pores of the freeze-dried scaffolds are interconnected, we conclude that in the frozen scaffolds,  
450 the polymer macro-network and the ice network are interlaced on the ice grain scale.

451 In perfect equiaxed growth, random orientation of the ice crystals within the scaffold is  
452 expected [36]. However, EBSD analysis (**Fig. 4E**) shows that the c-axis pole densities are  
453 higher in Z-direction. We infer that this preferred orientation is induced from the scaffold  
454 bottom. Indeed, needled branch crystals (as snow crystals) are substantially planar with c-axis  
455 orthogonal to that plane since growth kinetics in the basal plane is much larger than in c-axis  
456 direction [44]. Needled branch crystals which are parallel to the supporting plate (XY plane)  
457 are in the best thermal conditions to increase in thickness [34], which explains the observed  
458 anisotropy. Paradoxically, this preferred orientation (parallel to Z) is consistent with the  
459 preferential orientation of the pore, i.e. major axis parallel to XY plane, since growth is faster  
460 in the basal plane which presently coincides with XY plane.

461 The porosity decreases significantly between freeze-dried and swollen states, i.e. from  $\varepsilon =$   
462  $93 \pm 2\%$  down to  $\varepsilon = 29\% \pm 2\%$ . In the swollen state, the hydrogel porosity remains  
463 constant when increasing the solvent ionic strength even if the pores shrink. This remarkable  
464 result was confirmed by CLSM and two-photon microscopy of scaffolds prepared with FTIC-  
465 dextran.

466 A homogenous seeding of MC3T3-E1 cells within the pore network was achieved by the  
467 simple addition of a cell suspension on freeze-dried scaffolds. Isolated cells of different origins  
468 (species, tissues), two or more cell types, or cell clusters can be accommodated in these 3D  
469 porous scaffolds [17–19,21]. Such scaffolds are suitable for cell culture in 3D (especially when  
470 cell clustering and spheroid growth is necessary for studying cell development and  
471 differentiation), for tissue engineering or for pharmacological assays in 3D.

472

## 473 **5. Conclusions**

474 This study presented the mechanisms of pore formation during the freeze-drying of a cross-  
475 linked hydrogel at a low cooling rate and highlighted the interactions between the nano-scale  
476 polymer network and the growing ice crystals. We demonstrated the strong link between pore  
477 formation and the nucleation of ice.

478 The primary nucleation, heterogeneous and singular, occurs at significant supercooling. During  
479 recalescence, the rapidly growing ice needles fracture due to the constraints exerted by the  
480 surrounding nano-scale polymer network. The needle fragments induce secondary nucleation  
481 and a subsequent fine-grained polycrystalline structure. As freezing continues close to the ice  
482 melting point, the ice crystals get bigger, and reject the polymer in the intergranular space.  
483 Electron cryo-microscopy actually showed that the polymer chains segregate on the ice grain  
484 boundary network and form a macro-network. The characteristic length scale of the macro-  
485 network coincides with the ice grain size (160  $\mu\text{m}$ ) and is several orders of magnitude greater  
486 than the macromolecular correlation length (90 nm). Despite the scale separation between the  
487 mesh size and the ice grain size, we expect that a lower mesh size (obtained with a greater  
488 degree of cross-linking) should result in a lower grain size (and smaller macro-pores) since the  
489 secondary nucleation of ice would be enhanced.

490 After sublimation, ice grains are replaced by macro-pores (280  $\mu\text{m}$  mean size as measured by  
491 high-resolution X-ray tomography). The resulting dry structure is highly porous (93%). In the  
492 swollen state, the porosity decreases down to 29%. When the solvent ionic strength increases,  
493 the pores shrink (120  $\mu\text{m}$  in 0.025% NaCl and 54  $\mu\text{m}$  in DBPS) whereas the porosity remains  
494 constant. This remarkable result was confirmed by CLSM and two-photon microscopy. The  
495 scaffolds were further validated with the culture of pre-osteoblastic cells: the pores in the  
496 freeze-dried scaffold are adequately interconnected to allow homogenous cell seeding.

497 These findings should guide the strategies implemented to control the porous structure of  
498 hydrogel scaffolds.

499

## 500 **Acknowledgements**

501 This work is supported by the “IDI 2016” project funded by the IDEX Paris-Saclay, ANR-11-  
502 IDEX-0003-02. The authors acknowledge the 3D-BioMat project that is co-financed by the  
503 Grand Reims and the European Union with a total budget of 965,000€, hosted by the CEBB  
504 (51110 Pomacle, France) from 01/05/2016 to 30/04/2019. The authors acknowledge Dr Marie-  
505 Noëlle Labour and Cyril Breton for their kind help with two-photon microscopy and confocal  
506 microscopy, respectively. The authors acknowledge Isabelle Bataille for her help with the  
507 rheometer and Soraya Lanouar for the chemical characterizations of polymer batches.

508

## 509 **Conflict of Interest**

510 The authors declare that they have no conflict of interest.

## 511 **References**

- 512 [1] J.L. Drury, D.J. Mooney, Hydrogels for tissue engineering: scaffold design variables and  
513 applications, *Biomaterials*. 24 (2003) 4337–4351. doi:10.1016/S0142-9612(03)00340-5.  
514 [2] I.V. Yannas, J.F. Burke, P.L. Gordon, C. Huang, R.H. Rubenstein, Design of an artificial  
515 skin. II. Control of chemical composition, *J. Biomed. Mater. Res.* 14 (1980) 107–132.  
516 doi:10.1002/jbm.820140203.  
517 [3] F.J. O’Brien, B.A. Harley, I.V. Yannas, L.J. Gibson, The effect of pore size on cell  
518 adhesion in collagen-GAG scaffolds, *Biomaterials*. 26 (2005) 433–441.  
519 doi:10.1016/j.biomaterials.2004.02.052.  
520 [4] J.J. Campbell, A. Husmann, R.D. Hume, C.J. Watson, R.E. Cameron, Development of  
521 three-dimensional collagen scaffolds with controlled architecture for cell migration  
522 studies using breast cancer cell lines, *Biomaterials*. 114 (2017) 34–43.  
523 doi:10.1016/j.biomaterials.2016.10.048.  
524 [5] E. Sachlos, J. Czernuszka, Making Tissue Engineering Scaffolds Work. Review: The  
525 application of solid freeform fabrication technology to the production of tissue  
526 engineering scaffolds, *Eur. Cell. Mater.* 5 (2003) 29–40. doi:10.22203/eCM.v005a03.  
527 [6] L. Qian, H. Zhang, Controlled freezing and freeze drying: a versatile route for porous and  
528 micro-/nano-structured materials, *J. Chem. Technol. Biotechnol.* 86 (2011) 172–184.  
529 doi:10.1002/jctb.2495.

- 530 [7] N. Dagalakakis, J. Flink, P. Stasikelis, J.F. Burke, I.V. Yannas, Design of an artificial skin.  
531 Part III. Control of pore structure, *J. Biomed. Mater. Res.* 14 (1980) 511–528.
- 532 [8] H. Yoshida, T. Hatakeyama, H. Hatakeyama, Characterization of water in polysaccharide  
533 hydrogels by DSC, *J. Therm. Anal.* 40 (1993) 483–489. doi:10.1007/BF02546617.
- 534 [9] F. O’Brien, Influence of freezing rate on pore structure in freeze-dried collagen-GAG  
535 scaffolds, *Biomaterials.* 25 (2004) 1077–1086. doi:10.1016/S0142-9612(03)00630-6.
- 536 [10] H.-W. Kang, Y. Tabata, Y. Ikada, Fabrication of porous gelatin scaffolds for tissue  
537 engineering, *Biomaterials.* 20 (1999) 1339–1344. doi:10.1016/S0142-9612(99)00036-8.
- 538 [11] H. Zhang, I. Hussain, M. Brust, M.F. Butler, S.P. Rannard, A.I. Cooper, Aligned two- and  
539 three-dimensional structures by directional freezing of polymers and nanoparticles, *Nat.*  
540 *Mater.* 4 (2005) 787–793. doi:10.1038/nmat1487.
- 541 [12] H. Zhang, A.I. Cooper, Aligned Porous Structures by Directional Freezing, *Adv. Mater.*  
542 19 (2007) 1529–1533. doi:10.1002/adma.200700154.
- 543 [13] C.R. Rowland, L.A. Colucci, F. Guilak, Fabrication of anatomically-shaped cartilage  
544 constructs using decellularized cartilage-derived matrix scaffolds, *Biomaterials.* 91  
545 (2016) 57–72. doi:10.1016/j.biomaterials.2016.03.012.
- 546 [14] S. Deville, Freezing as a Path to Build Complex Composites, *Science.* 311 (2006) 515–  
547 518. doi:10.1126/science.1120937.
- 548 [15] T.M. Freyman, I.V. Yannas, L.J. Gibson, Cellular materials as porous scaffolds for tissue  
549 engineering, *Prog. Mater. Sci.* 46 (2001) 273–282. doi:10.1016/S0079-6425(00)00018-9.
- 550 [16] J.C. Fricain, S. Schlaubitz, C. Le Visage, I. Arnault, S.M. Derkaoui, R. Siadous, S. Catros,  
551 C. Lalande, R. Bareille, M. Renard, T. Fabre, S. Cornet, M. Durand, A. Léonard, N.  
552 Sahraoui, D. Letourneur, J. Amédée, A nano-hydroxyapatite – Pullulan/dextran  
553 polysaccharide composite macroporous material for bone tissue engineering,  
554 *Biomaterials.* 34 (2013) 2947–2959. doi:10.1016/j.biomaterials.2013.01.049.
- 555 [17] C. Ehret, R. Aid-Launais, T. Sagardoy, R. Siadous, R. Bareille, S. Rey, S. Pechev, L.  
556 Etienne, J. Kalisky, E. de Mones, D. Letourneur, J. Amedee Vilamitjana, Strontium-  
557 doped hydroxyapatite polysaccharide materials effect on ectopic bone formation, *PLOS*  
558 *ONE.* 12 (2017) e0184663. doi:10.1371/journal.pone.0184663.
- 559 [18] J.C. Fricain, R. Aid, S. Lanouar, D.B. Maurel, D. Le Nihouannen, S. Delmond, D.  
560 Letourneur, J. Amedee Vilamitjana, S. Catros, In-vitro and in-vivo design and validation  
561 of an injectable polysaccharide-hydroxyapatite composite material for sinus floor  
562 augmentation, *Dent. Mater.* 34 (2018) 1024–1035. doi:10.1016/j.dental.2018.03.021.
- 563 [19] J. Guerrero, H. Oliveira, R. Aid, R. Bareille, R. Siadous, D. Letourneur, Y. Mao, J. Kohn,  
564 J. Amédée, Influence of the three-dimensional culture of human bone marrow  
565 mesenchymal stromal cells within a macroporous polysaccharides scaffold on Pannexin  
566 1 and Pannexin 3, *J. Tissue Eng. Regen. Med.* 12 (2018) e1936–e1949.  
567 doi:10.1002/term.2625.
- 568 [20] S. Lanouar, R. Aid-Launais, A. Oliveira, L. Bidault, B. Closs, M.-N. Labour, D.  
569 Letourneur, Effect of cross-linking on the physicochemical and in vitro properties of  
570 pullulan/dextran microbeads, *J. Mater. Sci. Mater. Med.* 29 (2018). doi:10.1007/s10856-  
571 018-6085-x.
- 572 [21] E.J. Ribot, C. Tournier, R. Aid-Launais, N. Koonjoo, H. Oliveira, A.J. Trotier, S. Rey, D.  
573 Wecker, D. Letourneur, J. Amedee Vilamitjana, S. Miraux, 3D anatomical and perfusion  
574 MRI for longitudinal evaluation of biomaterials for bone regeneration of femoral bone  
575 defect in rats, *Sci. Rep.* 7 (2017) 6100. doi:10.1038/s41598-017-06258-0.
- 576 [22] S. Piazzolo, M. Montagnat, J.R. Blackford, Sub-structure characterization of  
577 experimentally and naturally deformed ice using cryo-EBSD, *J. Microsc.* 230 (2008) 509–  
578 519. doi:10.1111/j.1365-2818.2008.02014.x.

- 579 [23] M. Montagnat, T. Chauve, F. Barou, A. Tommasi, B. Beausir, C. Fressengeas, Analysis  
580 of Dynamic Recrystallization of Ice from EBSD Orientation Mapping, *Front. Earth Sci.*  
581 3 (2015) 81. doi:10.3389/feart.2015.00081.
- 582 [24] A. Autissier, C.L. Visage, C. Pouzet, F. Chaubet, D. Letourneur, Fabrication of porous  
583 polysaccharide-based scaffolds using a combined freeze-drying/cross-linking process,  
584 *Acta Biomater.* 6 (2010) 3640–3648. doi:10.1016/j.actbio.2010.03.004.
- 585 [25] D. İmren, M. Gümüşderelioğlu, A. Güner, Synthesis and characterization of dextran  
586 hydrogels prepared with chlor- and nitrogen-containing crosslinkers, *J. Appl. Polym. Sci.*  
587 102 (2006) 4213–4221. doi:10.1002/app.24670.
- 588 [26] K. Nishinari, K. Kohyama, P.A. Williams, G.O. Phillips, W. Burchard, K. Ogino,  
589 Solution properties of pullulan, *Macromolecules.* 24 (1991) 5590–5593.  
590 doi:10.1021/ma00020a017.
- 591 [27] K. Kendall, *Molecular Adhesion and Its Applications: the Sticky Universe*, Springer US,  
592 Boston, MA, 2004. <http://public.eblib.com/choice/publicfullrecord.aspx?p=3036018>  
593 (accessed August 31, 2018).
- 594 [28] L.R.G. Treloar, *The Physics of rubber elasticity*, Clarendon Press, Oxford, 2005.  
595 <http://www.myilibrary.com?id=134637> (accessed January 10, 2019).
- 596 [29] N.A. Peppas, E.W. Merrill, Crosslinked poly(vinyl alcohol) hydrogels as swollen elastic  
597 networks, *J. Appl. Polym. Sci.* 21 (1977) 1763–1770. doi:10.1002/app.1977.070210704.
- 598 [30] G.S. Buliga, D.A. Brant, Temperature and molecular weight dependence of the  
599 unperturbed dimensions of aqueous pullulan, *Int. J. Biol. Macromol.* 9 (1987) 71–76.  
600 doi:10.1016/0141-8130(87)90029-8.
- 601 [31] T. Canal, N.A. Peppas, Correlation between mesh size and equilibrium degree of swelling  
602 of polymeric networks, *J. Biomed. Mater. Res.* 23 (1989) 1183–1193.  
603 doi:10.1002/jbm.820231007.
- 604 [32] G. Vali, Freezing Rate Due to Heterogeneous Nucleation, *J. Atmospheric Sci.* 51 (1994)  
605 1843–1856. doi:10.1175/1520-0469(1994)051<1843:FRDTHN>2.0.CO;2.
- 606 [33] H.R. Pruppacher, J.D. Klett, *Microphysics of Clouds and Precipitation*, *Nature.* 284  
607 (1980) 88–88. doi:10.1038/284088b0.
- 608 [34] P.V. Hobbs, *Ice physics*, Oxford, Clarendon Press, 1974.
- 609 [35] G. Vali, Repeatability and randomness in heterogeneous freezing nucleation,  
610 *Atmospheric Chem. Phys.* 8 (2008) 5017–5031.
- 611 [36] M. Schremb, C. Tropea, Solidification of supercooled water in the vicinity of a solid wall,  
612 *Phys. Rev. E.* 94 (2016) 052804. doi:10.1103/PhysRevE.94.052804.
- 613 [37] S.V. Alekseenko, C. Mendig, M. Schulz, M. Sinapius, O.A. Prykhodko, An experimental  
614 study of freezing of supercooled water droplet on solid surface, *Tech. Phys. Lett.* 42  
615 (2016) 524–527. doi:10.1134/S1063785016050187.
- 616 [38] M. Cassanelli, I. Norton, T. Mills, Role of gellan gum microstructure in freeze drying and  
617 rehydration mechanisms, *Food Hydrocoll.* 75 (2018) 51–61.  
618 doi:10.1016/j.foodhyd.2017.09.013.
- 619 [39] ASTM F2450-18, *Standard Guide for Assessing Microstructure of Polymeric Scaffolds*  
620 *for Use in Tissue-Engineered Medical Products*, ASTM International, 2018.  
621 doi:10.1520/F2450-18.
- 622 [40] A. Fernández-Nieves, A. Fernández-Barbero, F.J. de las Nieves, Salt effects over the  
623 swelling of ionized mesoscopic gels, *J. Chem. Phys.* 115 (2001) 7644–7649.  
624 doi:10.1063/1.1403002.
- 625 [41] L. Klembt Andersen, S. Antoranz Contera, J. Justesen, M. Duch, O. Hansen, J. Chevallier,  
626 M. Foss, F. Pedersen, F. Besenbacher, Cell volume increase in murine MC3T3-E1 pre-  
627 osteoblasts attaching onto biocompatible Tantalum observed by magnetic AC mode

- 628 Atomic Force Microscopy, *Eur. Cell. Mater.* 10 (2005) 61–69.  
629 doi:10.22203/eCM.v010a07.
- 630 [42] A.A. Shibkov, Yu.I. Golovin, M.A. Zheltov, A.A. Korolev, A.A. Leonov, Morphology  
631 diagram of nonequilibrium patterns of ice crystals growing in supercooled water, *Phys.*  
632 *Stat. Mech. Its Appl.* 319 (2003) 65–79. doi:10.1016/S0378-4371(02)01517-0.
- 633 [43] S.G. Agrawal, A.H.J. Paterson, Secondary Nucleation: Mechanisms and Models, *Chem.*  
634 *Eng. Commun.* 202 (2015) 698–706. doi:10.1080/00986445.2014.969369.
- 635 [44] H. Nada, Y. Furukawa, Anisotropy in growth kinetics at interfaces between proton-  
636 disordered hexagonal ice and water: A molecular dynamics study using the six-site model  
637 of H<sub>2</sub>O, *J. Cryst. Growth.* 283 (2005) 242–256. doi:10.1016/j.jcrysgro.2005.05.057.  
638